RSC Advances

PAPER

View Article Online
View Journal | View Issue

Cite this: *RSC Adv.*, 2025, **15**, 47619

Effect of vanadium (V) doping on the physical characteristics of novel n-type TiO_2 for sustainable energy storage

A. Timoumi,*[a] Ziad Moussa,[b] Hatem M. Altass,[c] Khalid Althagafy,[a] Abdulrahman A. Alsimaree,[d] Munirah M. Al-Rooqi,[c] Rabab S. Jassas[e] and Saleh A. Ahmed *[cf]

The design of high-performance advanced materials for green energy nanotechnology is vital for progress in cutting-edge domains such as environmental sustainability and energy conversion technologies. In this study, we report the synthesis and characterization of undoped and vanadium-doped titanium dioxide (TiO_2) in both pellet and thin film forms. The influence of vanadium doping levels on the material's physical and electrical properties was systematically investigated. Structural, morphological, compositional, electrical, and optical analyses were performed using X-ray diffraction (XRD), scanning electron microscopy (SEM), X-ray photoelectron spectroscopy (XPS), impedance spectroscopy (IS) (for pellets) and UV-visible spectroscopy (for films). XRD results confirmed that all samples were polycrystalline in the anatase phase, while increasing vanadium content reduced crystallite size and enhanced density. While the elemental composition remained relatively stable, XPS data showed the formation of Ti^{3+} states and oxygen vacancies, which play a pivotal role in modifying electronic behavior. Impedance spectroscopy indicated semiconducting behavior, with resistance decreasing as temperature increased, reflecting enhanced conductivity. Optical studies (UV-vis spectroscopy) showed a redshift in the absorption edge toward the visible region, with a reduction in bandgap energy from 3.20 eV (undoped) to 2.85 eV (6% V-doped), attributed to localized states and the formation of impurity bands. Electrical measurements showed enhanced conductivity with temperature and a clear transition to non-Debye behavior, reflecting a distribution of relaxation times likely due to grain boundaries and defect states. Notably, the dielectric constant was significantly elevated, supporting potential use in energy storage or solar energy applications. This work provides key insights into tailoring TiO_2-based materials through metal doping for sustainable energy storage.

Received 2nd November 2025
Accepted 24th November 2025

DOI: 10.1039/d5ra08419a

rsc.li/rsc-advances

1. Introduction

The evolution of solar cell technologies is broadly categorized into three main generations: silicon-based, thin-film, and organic solar cells.[1–3] Among these, thin-film solar cells have reached commercial maturity, with global production reaching 30 GW. Despite this progress, ongoing research is driven by the need to develop solar cells that are not only highly efficient but also cost-effective and environmentally sustainable.[4] Transparent conducting oxide (TCO) materials have drawn considerable attention due to their favorable physical, chemical, optical, and optoelectronic properties. Among these, titanium dioxide (TiO_2) is chosen, owing to its high refractive index, chemical stability, low cost, non-toxicity, and excellent photocatalytic activity.[5] Thin films of TiO_2 are especially advantageous in electronic, photonic, and optoelectronic applications, as the material properties at reduced dimensions often outperform their bulk counterparts.[6] TiO_2 exists in several polymorphic forms, primarily anatase, rutile, and brookite, with direct optical bandgaps of approximately 3.2 eV, 3.4 eV, and 3.37 eV, respectively.[7] Among these, the anatase phase is generally considered the most photoactive for photocatalytic applications.[8] The deposition of TiO_2 thin films is fundamental across various technological fields, and numerous fabrication methods have been developed to tailor these films for specific applications.[9–13] Doping TiO_2 with metal ions is a well-established strategy to tune its interfacial electron transport and

[a]*Department of Physics, Faculty of Science, Umm Al-Qura University, 24382, Makkah, Saudi Arabia. E-mail: aotemoume@uqu.edu.sa*

[b]*Department of Chemistry, College of Science, United Arab Emirates University, P. O. Box 15551, Al Ain, United Arab Emirates*

[c]*Department of Chemistry, Faculty of Science, Umm Al-Qura University, 21955, Makkah, Saudi Arabia*

[d]*Department of Chemistry, College of Science and Humanities, Shaqra University, Shaqra, Saudi Arabia*

[e]*Department of Chemistry, Jamoum University College, Umm Al-Qura University, 21955 Makkah, Saudi Arabia*

[f]*Chemistry Department, Faculty of Science, Assiut University, 71516 Assiut, Egypt. E-mail: saahmed@uqu.edu.sa; saleh_63@hotmail.com*

enhance photoreactivity.[12–14] Metal ion doping, such as with Fe, Ag, Zn, Cu, or V has been shown to significantly modify the structural, optical, and electrical properties of TiO_2 thin films.[15–20] In particular, dopants like Nb, Fe, and Zn are known to reduce TiO_2's wide bandgap, making it responsive to visible light, a key requirement for solar energy conversion.[21–23] Doping TiO_2 with transition elements having high oxidation states (such us; Mo^{6+}, Nb^{5+}, W^{6+}, V^{5+}) shows good photo catalytic characteristics than doping with transition elements having lower oxidation states (such us; Fe^{3+}, Co^{2+}, Ni^{2+}). This is the result of a larger number of hydroxyl groups on the surface, which makes such surfaces more photocatalytically active.

Among these dopants, vanadium (V) remains relatively underexplored. Due to its similar ionic radius to titanium, V is a suitable dopant that can substitute into Ti sites in the TiO_2 lattice.[24] Vanadium enhances visible light absorption[25] and facilitates charge separation by reducing charge–hole recombination. Furthermore, it may assist in the transport of photoexcited electrons across the surface, thus enhancing the material's photocatalytic and optoelectronic performance.

Vanadium may be readily doped into TiO_2 because its ionic radius is nearly identical to that of titanium.[26] As a result, numerous scientists have created V-doped TiO_2 and investigated its photocatalytic characteristics. According to Klosek and Raftery,[26] ethanol can be photodegraded by V-doped TiO_2 when exposed to visible light. TiO_2 catalysts were altered by Anpo *et al.*[27] by subjecting them to high energy metal ion bombardment. The V ion was more effective in the red shift, and the metal ion-implanted TiO_2 exhibited a significant absorption shift toward the visible light band. V-doped TiO_2 with visible activity was created by Zhou *et al.*[28] using ion implantation and modified sol–gel techniques, respectively. Although vanadium and vanadium-based compounds have several advantages in energy storage and photocatalysis, there are several drawbacks, mainly with regard to mass transport constraints, structural stability, and charge carrier recombination.[29]

Herein, we intend to clarify the role of vanadium in the structural, the morphological, the optical, and the electronic properties of undoped and vanadium-doped TiO_2, with particular focus on the influence of varying vanadium amounts. Commercially available TiO_2 powder was doped with vanadium and separately processed into pellets and thin films for further investigation. Through obtained detailed characterization, we assessed the feasibility of using these readily available samples as a practical and economical source material. To the best of our knowledge, this work introduces also a novel and efficient route for optimizing thin film fabrication conditions for physical vapor deposition (PVD)-based applications or sustainable energy storage.

2. Materials, synthesis and characterizations

2.1 Materials

Titanium dioxide (TiO_2, 99.5% purity, CAS No. 13463-67-7) and vanadium(II) chloride (VCl_2, 99% purity, CAS No. 10580-52-6) were purchased from Sigma-Aldrich. For pellet formation, the powders were thoroughly mixed and compressed into cylindrical pellets (8 mm diameter) using a stainless-steel mold equipped with a punch and counter-punch to ensure uniform compaction.

2.2 Synthesis of thin films and pellets samples

TiO_2 powder (5 g) was dispersed in 50 mL of deionized water and stirred for 30 minutes at room temperature (27 °C) to form a uniformly dispersed white suspension. Vanadium(II) chloride was then added in varying amounts (0.0, 0.2, 0.3, and 0.4 g) to obtain doped samples. The V-doping content in TiO_2 is expressed as a percentage of weight of the base amount of titanium oxide, which is 5 grams. The following ratios represent the proportion of VCl_2 to the basic amount of TiO_2 (0%, 4%, 6% and 8%). The activator content (V) in TiO_2 is expressed as a percentage by weight of the base amount of titanium oxide, which is 5 grams.

The resulting mixtures were sonicated to enhance homogeneity and then applied to clean glass substrates using a spin coating process. Each layer was deposited by spinning at 6000 rpm for 30 seconds, followed by a brief drying period using mild heating. Multiple layers were applied in a stepwise manner to achieve uniform film coverage. After that, samples are annealed on hot plate at 300 °C for about 15 min. The average final thickness is estimated to be about 300 nm for all samples. The acquired samples are nearly homogeneous and uniform. Therefore, the deposition technique and doping process which can be impacted by elements like dopant concentration and precursor solution stability determine the uniformity of doped films. For pellet, the dried mixtures were pressed into mold (stainless steel with punch and counter-punch) using a uniaxial hydraulic press at 6000 psi (41.4 MPa) for a few minutes. Each sample was compressed into a pellet with a diameter of 12 mm and a thickness of 1 mm, measured using a Vernier caliper. A total of four distinct sample sets were prepared. Pellets are placed in a programmable furnace allowing the temperature to be adjusted and fixed during measurements of the electrical characteristics. The atmosphere of the furnace is air and the heating time of the pellets to measure the results is almost 30 minutes. The overall synthesis process is illustrated in Fig. 1.

2.3 Methods of characterization

The crystal structure of the samples was analyzed using X-ray diffraction (XRD) with a Unisantis XRD-300 analyzer, employing Cu-Kα radiation (λ = 0.15406 nm) and a graphite monochromator. Scans were performed over a 2θ range of 10° to 70°. X-ray photoelectron spectroscopy (XPS) was conducted using a JPS-9030 spectrometer equipped with an Al-Kα X-ray source (photon energy = 1487 eV). All binding energies were referenced to the C 1s peak at 284.6 eV. Surface morphology was examined using scanning electron microscopy (SEM). The quantitative elemental composition of the films was analyzed *via* EDX. Optical properties were evaluated at room temperature using a UVD-2950 double-beam UV-Vis spectrophotometer over the wavelength range of 200–1100 nm. Electrical AC conductance

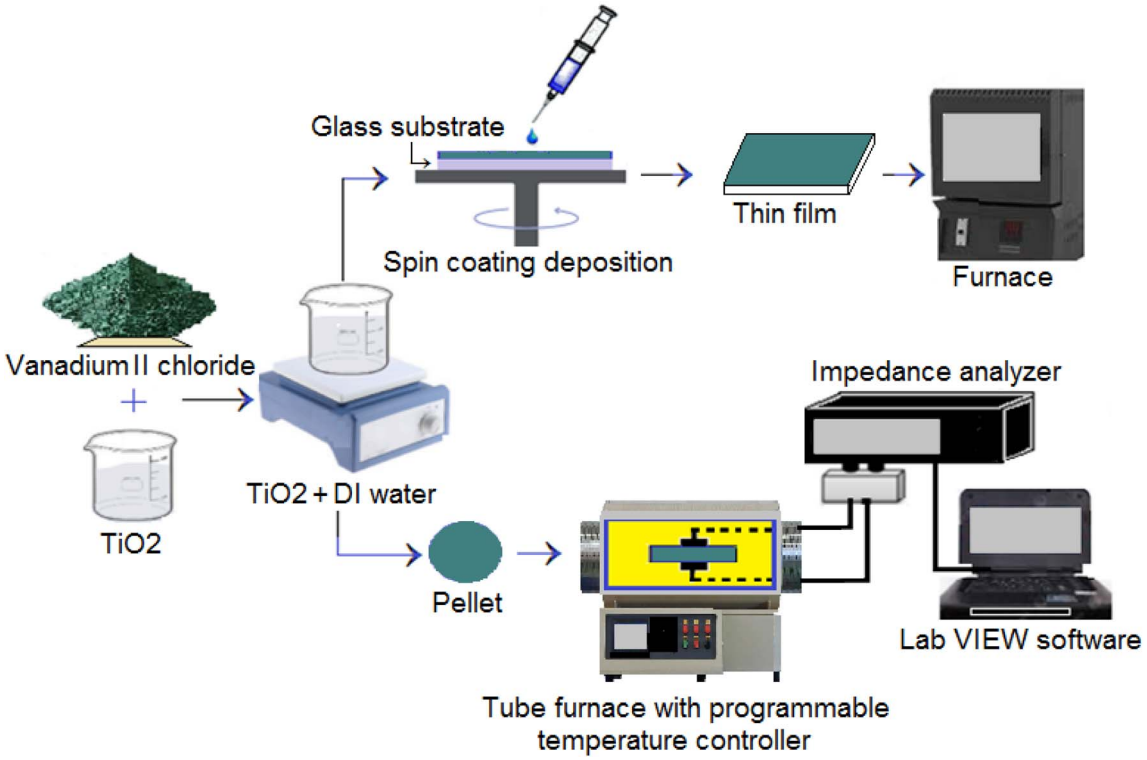

Fig. 1 Schematic diagram illustrating the setup of the impedance spectroscopy device.

was measured using the setup shown in Fig. 1. Frequency-dependent conductivity measurements were performed at ambient temperature, while temperature-dependent measurements were conducted in the range of 280 °C to 500 °C, in 20 °C increments. An Agilent 4294A impedance analyzer was used to record conductance after thermal equilibrium was reached at each step, with a temperature tolerance of ±2 °C. LabVIEW software was used to control experimental parameters and collect data, except for the temperature control which was *via* the programmable oven.

3 Results and discussion

3.1 Diffraction measurements of X-rays

The crystallographic properties of undoped and vanadium-doped TiO_2 samples were analyzed using X-ray diffraction (XRD) over a 2θ scan range of 10° to 70°, as shown in Fig. 2. The diffraction patterns of all samples closely matched the standard pattern of the anatase phase of TiO_2, indicating that the fundamental crystal structure remained unaltered by doping. No additional peaks corresponding to secondary phases or vanadium oxides were detected, suggesting successful incorporation of vanadium without significant structural disruption. Using the Scherrer equation, the average crystallite size (D) of the films was estimated from the XRD data:[30]

$$D = \frac{k\lambda}{\beta \cos \theta} \quad (1)$$

where D is the crystallite size, k is the shape factor, λ is the X-ray wavelength, β is the full width at half maximum (FWHM) of the diffraction peak, and θ is the Bragg angle. The estimation was based on the FWHM of the (110) diffraction peak and yielded an average crystallite size of approximately 14 nm. The slight reduction in crystallite size upon doping can be attributed to the presence of vanadium, which inhibits grain growth during the nitrogen adsorption measurements[31] and the surface becomes

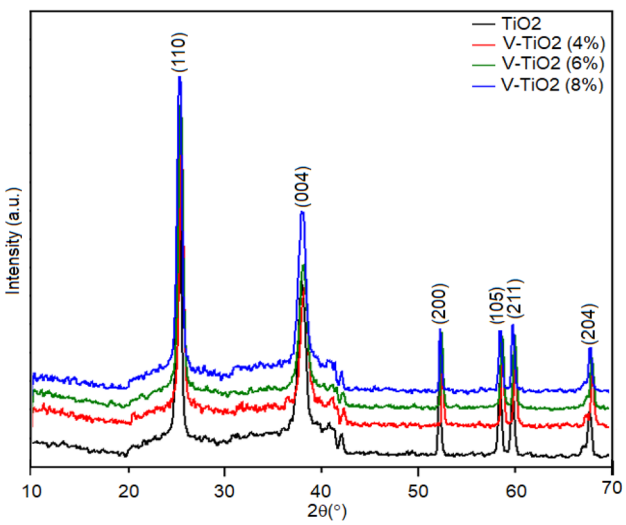

Fig. 2 X-ray diffraction (XRD) patterns of undoped and V-doped TiO_2 samples with varying vanadium-doping levels.

more densely packed. This tendency, which is associated with the addition of V^{3+} ions to the TiO_2 lattice, causes lattice strain and defects, which result in the creation of finer grains.

Furthermore, the XRD patterns revealed minor shifts in 2θ values with increasing dopant concentrations, suggesting lattice distortion caused by the incorporation of vanadium ions into the TiO_2 crystal lattice. This substitution may influence the crystal structure and induce strain. Enhanced structural integrity and increased carrier mobility observed in doped TiO_2 samples indicate that vanadium doping not only affects crystallite size but also contributes to improved thermal and electronic stability.[32] Reducing crystallite size improves film thickness, boosts photocatalytic activity, and prevents photo-excited electron–hole pair recombination. These findings suggest that vanadium incorporation enhances both structural and functional properties of TiO_2.

According to JCPDS Card No. 65-5714, the XRD peaks observed at 25.50°, 37.81°, 51.91°, 58.61°, 59.71°, and 67.32° represent the (110), (004), (200), (105), (211), and (204) planes of the anatase phase of TiO_2, respectively. These characteristic reflections confirm that both the undoped and V-doped TiO_2 samples maintain the anatase crystal structure. Vanadium segregation at grain boundaries could be the cause of the lack of subsequent phases. This implies that vanadium considerably disturbs the normal crystal structure at higher activation levels, resulting in a more intricate and uneven surface shape.

3.2 Surface morphology testing

3.2.1 SEM analysis. SEM images were collected to investigate the morphology of the synthesized samples. As shown in Fig. 3, the samples primarily consist of aggregated nanoparticles. The surface roughness has significantly increased in this figure. The incorporation of vanadium alter the surface morphology. The SEM images of undoped TiO_2 (Fig. 3a) and V-doped samples 4%, 6%, and 8% (Fig. 3b–d, respectively), exhibit comparable nanoparticle morphology, indicating that vanadium doping impact the overall structural appearance of the material. Thus, at high doping levels, particle aggregation could occur. High doping levels can cause phase segregation, decreased solubility, and the development of dopant-rich domains or bigger aggregates in a variety of materials, especially organic semiconductors and solutions. The space charge layer width can be decreased by high doping, but this effect can be reversed by nanostructuring, enabling volume fractions that are comparable to those of larger, low-doped particles. In applications like photocatalysis and batteries, this can enhance overall performance.

3.2.2 EDX analysis. The materials' quantitative composition was examined using energy dispersive X-ray analysis (EDX). The atomic percentages for each sample are displayed in Table 1, which indicates that V atoms are present in the TiO_2 lattice.

3.3 XPS analysis

The elemental compositions and chemical states of each constituent element were investigated using X-ray Photoelectron Spectroscopy (XPS). The XPS measurements revealed the surface chemical composition and valence states. Fig. 4 displays the full survey spectrum of the pure TiO_2 sample. Several peaks appear within the 0–800 eV binding energy range. The XPS survey confirmed the presence of titanium (Ti), oxygen (O), and carbon (C) in the sample. The C 1s peak, consistently observed at 284.6 eV, is usually attributed to the adventitious carbon or carbon residues from the organic precursor. All samples showed distinct peaks corresponding to C 1s, O 1s, and Ti 2p. The high-resolution Ti 2p spectrum of the undoped TiO_2 (Fig. 4a) exhibited characteristic Ti^{4+} signals at ~458 eV (Ti $2p_{3/2}$) and ~464 eV (Ti $2p_{1/2}$), confirming the anatase phase. In doped samples, a slight shift in the Ti 2p peaks toward higher binding energies was observed, which may be attributed to partial reduction of Ti^{4+} due to localized electrons at oxygen vacancy (V_o) sites.[33,34] Additionally, peak broadening in the Ti 2p region for doped samples indicates the presence of smaller crystallites, consistent with XRD results.

Fig. 4b displays the high-resolution spectrum of Ti 2p. The spin–orbit splitting of this doublet results in two distinct peaks: Ti $2p_{3/2}$ (binding energy at 459.8 eV) and Ti $2p_{1/2}$ (binding energy at 465.5 eV), corresponding to the Ti^{4+} oxidation state in the TiO_2 lattice.[35] Fig. 4c shows the high-resolution O 1s spectra for the samples, exhibiting two main components. The lattice oxygen (O^{2-}) in TiO_2 is represented by the peak at ~530 eV, while surface hydroxyl groups (Ti–OH) or adsorbed oxygen

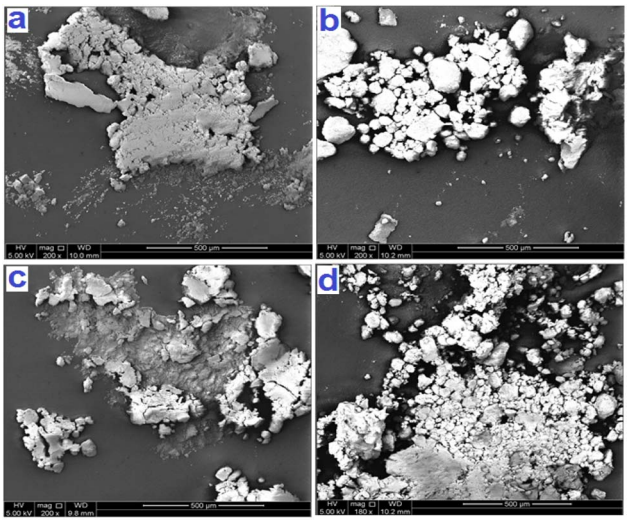

Fig. 3 SEM images of (a) undoped TiO_2, (b) 4V-doped TiO_2, (c) 6V-doped TiO_2, and (d) 8V-doped TiO_2 samples.

Table 1 Atomic composition of samples

	Mass atomic (%)		
Sample	Ti	O	V
TiO_2	13.93	86.07	—
4% V-doped TiO_2	10.46	88.78	0.63
6% V-doped TiO_2	12.37	85.38	1.79
8% V-doped TiO_2	11.98	83.92	3.49

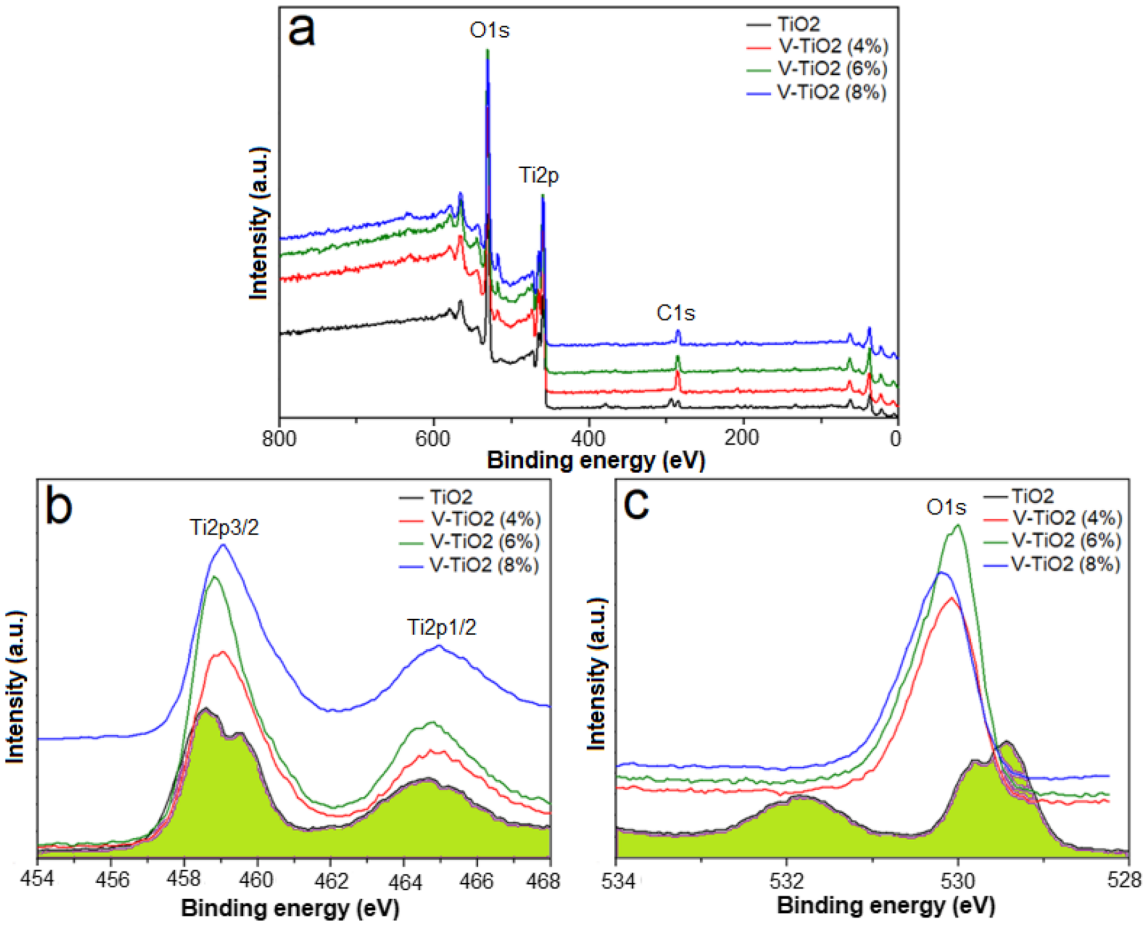

Fig. 4 (a) XPS survey spectra of pure TiO_2 and V-doped TiO_2 samples, showing the elemental composition, and high-resolution spectra of (b) Ti 2p peaks and (c) O 1s peaks.

species are responsible for the peak at 538 eV.[36,37] These surface-related oxygen species are crucial for photocatalysis, as they can trap photogenerated holes and facilitate the formation of highly reactive hydroxyl radicals, which play a significant role in the degradation of organic contaminants.[38] The presence of peak in the TiO_2 sample at 529.5 eV suggests the existence of oxygen vacancies (V_o) and surface Ti–OH species, which enhance photocatalytic activity by improving charge separation and extending visible-light absorption.[39,40] These oxygen-related defects are therefore crucial contributors to the observed photocatalytic behavior of the pure and doped TiO_2 powder. By creating defect states that reduce the band gap, allowing visible light absorption and offering locations for charge carrier separation, the creation of Ti^{3+} and oxygen vacancies (OVs) in TiO_2 enhances photocatalytic and electrical activity.

3.4 Analysis of electrical characteristics

Impedance spectroscopy (IS) was employed to investigate the dielectric behavior of pure and V-doped TiO_2 samples as a function of temperature. To enable measurements, the pellets were coated with electrodes connected to copper wires. The Nyquist diagrams (Z'' *vs.* Z') reveal a decline in resistance with increasing temperature, which can be attributed to the thermal activation of charge carriers. A decrease in the semicircular arc width at elevated temperatures indicates enhanced conductivity.[41] Moreover, variations in the width and shape of the semicircles with temperature are characteristic of typical semiconducting behavior.[42] To determine whether the observed abnormal dielectric relaxation (ADR)[43] is associated with the positive temperature coefficient of resistance (PTCR) effect due to a metal–insulator transition (MIT) influenced by humidity,[44] Nyquist plots were recorded, as shown in Fig. 5. In these plots, Z' and Z'' represent the real and imaginary components of the complex impedance (Z^*), respectively. The Nyquist diagrams exhibit distinct features for undoped and V-doped TiO_2. The large semicircular arc in the high-frequency region, which ends at the origin, corresponds to the bulk (grain) response. In contrast, a short linear tail in the low-frequency region represents the interfacial or electrode polarization response. This tail is attributed to Warburg impedance.[45] The Warburg component becomes more pronounced at 300 °C and diminishes at higher temperatures, consistent with the desorption of water molecules from the surface. As temperature increases, the main semicircular arc expands, indicating PTCR behavior.[46] The impedance response can be modeled by an equivalent circuit consisting of a resistor (R) and a capacitor (C) connected in

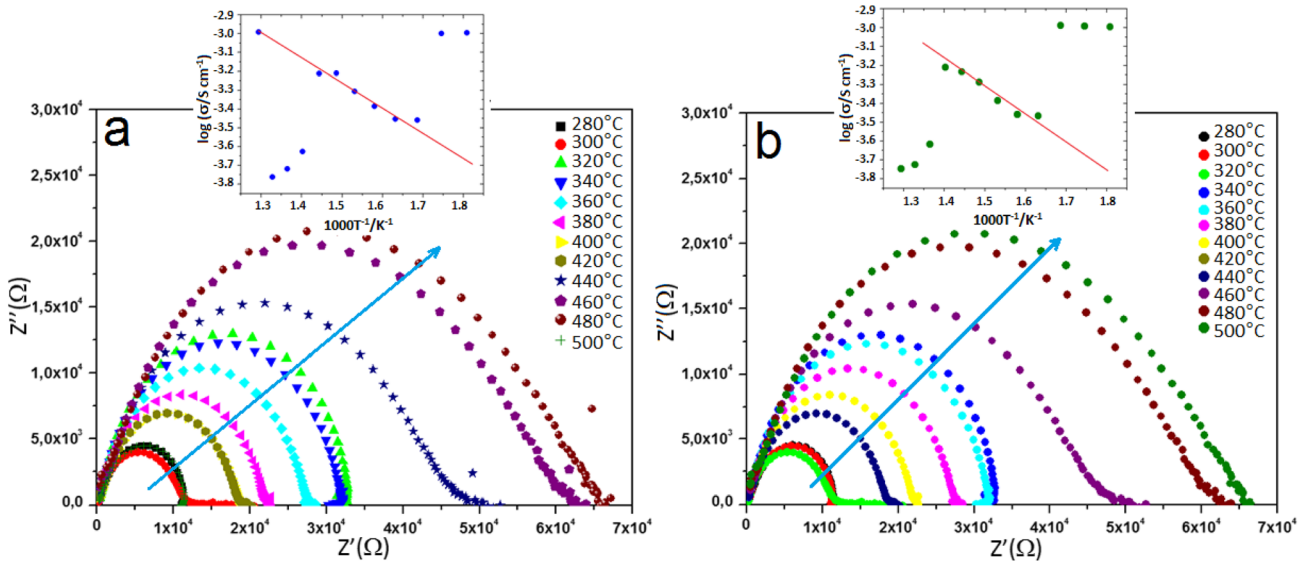

Fig. 5 Nyquist plots (Z'' *vs.* Z') showing the impedance response of (a) undoped and (b) 8% V-doped TiO_2 pellets.

parallel.[47] For such a system, the imaginary component of the impedance is given by:

$$Z'' = R\frac{\omega\tau}{1-(\omega\tau)^2} \quad (2)$$

where the relaxing time is indicated by $\tau = RC$ and the angular frequency by $\omega = 2\pi f$. At the frequency where $\omega\tau = 1$, a peak with an intensity of $R/2$ is observed in the imaginary section of the impedance. The Nyquist plots can also be used to extract the resistance and relaxation time values at different temperatures, providing insights into the electrical conduction mechanisms and relaxation phenomena of the materials.

The experimental values of electrochemical conductivity (σ) were calculated for both the TiO_2 and V-TiO_2 samples (pellet form) using the eqn (3). In this equation, L represents the pellet thickness, S denotes the area of the silver electrode, and R stands for the fitted resistance value from Nyquist plots.

$$\sigma = L/SR \quad (3)$$

The variation of the real part of impedance (Z') with frequency at different temperatures is shown in Fig. 6. At lower frequencies, Z' increases due to dominant polarization effects, which lead to higher resistance.[48,49] Because ions and electrons move more readily at higher temperatures, resistance typically decreases. Temperature influences impedance by affecting the speed of chemical and physical processes. Impedance, particularly the real component, varies throughout the spectrum, with low- and mid-frequency regions frequently displaying a larger reliance on temperature. As the temperature rises, thermal activation of charge carriers results in a decrease in Z', particularly at higher frequencies where the values tend to converge. This behavior indicates enhanced conductivity with increasing temperature and is characteristic of semiconducting materials. Impedance analysis revealed thermally stimulated conduction

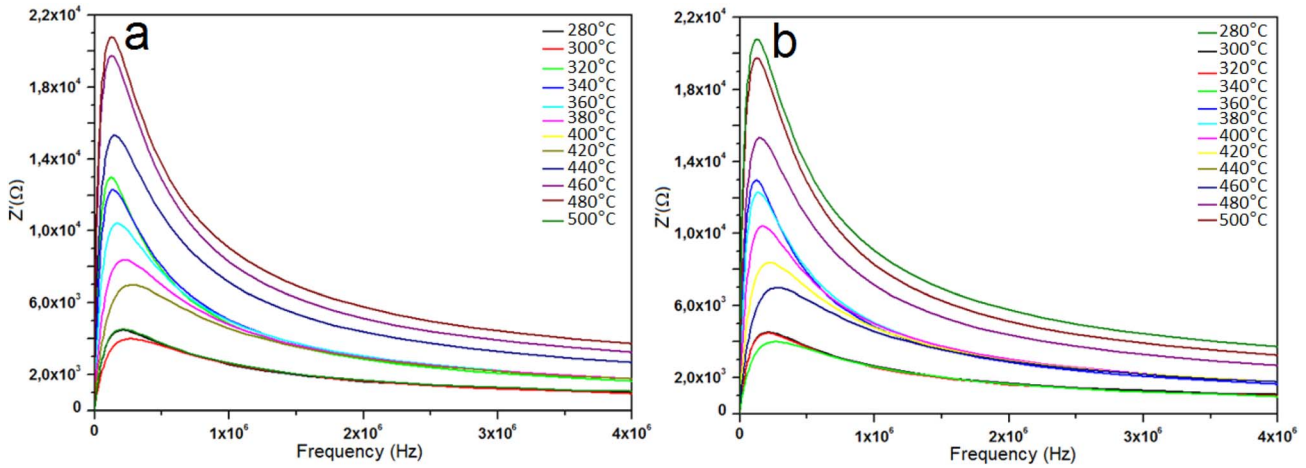

Fig. 6 Real part of impedance (Z') *vs.* frequency of (a) undoped and (b) 8% V-doped TiO_2 pellets.

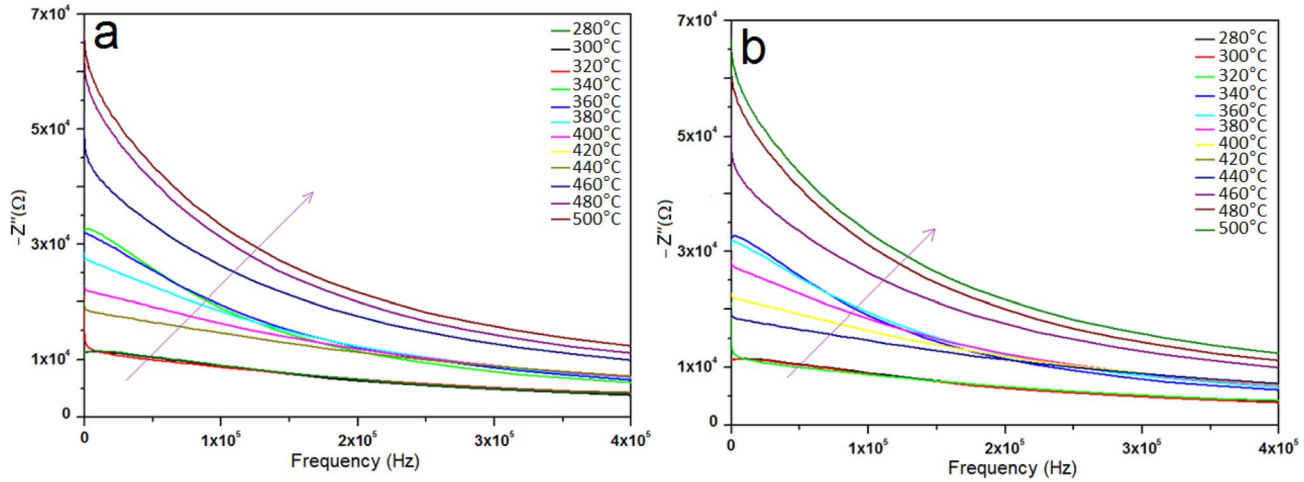

Fig. 7 Imaginary part of impedance (Z'') *vs.* frequency of (a) undoped and (b) 8% V-doped TiO_2 pellets.

and non-Debye behavior (non-exponential relaxation processes). Defect states and particle/grain boundaries can be linked to this occurrence. Particle and grain boundaries may cause non-ideal relaxation because of differences in conductivity and resistance between the bulk material and the boundaries.

The variation of the imaginary part of impedance (Z'') with frequency at different temperatures is shown in Fig. 7. As frequency increases, Z'' initially rises, reaching a maximum at a characteristic relaxation frequency, then decreases. This peak corresponds to the relaxation time of the system. With increasing temperature, the Z'' values decrease, indicating a reduction in resistance due to enhanced charge carrier mobility. The observed shift in the relaxation peak with temperature reflects the influence of thermal activation on the electrical relaxation behavior of the samples.[50–52]

3.5 Optical analysis of V-TiO_2 thin films

Understanding the optical characteristics of materials is necessary for the design and assessment of optoelectronic devices. To assess the impact of vanadium incorporation on the optical behavior of TiO_2 thin films, we investigated their transmittance and absorbance spectra across the wavelength range of 250–1100 nm. Fig. 8a illustrates the optical transmittance profiles of both undoped and V-doped TiO_2 films at various doping levels. The undoped films exhibited strong absorption in the UV and visible regions (250–600 nm), with negligible transmittance, indicating minimal photon penetration. Upon V doping, the absorption edge initially shifted toward shorter wavelengths (blue shift), which is attributed to the Burstein–Moss effect.[53] Under these conditions, the introduction of vanadium increases the density of free carriers. Vanadium atoms introduce localized states near the conduction band, increasing electronic band tailing and promoting sub-bandgap absorption, thereby narrowing the effective optical bandgap. Additionally, V doping had a pronounced effect on transmittance. An initial improvement in transparency was observed, particularly in the visible region, where transmittance exceeded 50% at an optimal doping level. At higher doping concentrations, however, transmittance declined significantly (down to ~15%), likely due to increased light scattering and absorption from defects, grain boundaries, or carrier-induced intraband transitions. This suggests that structural or electrical alterations brought on by excessive doping may impair optical transparency. Film thickness affects the ratio of optical transparency to light absorption, which has an impact on solar cells and energy storage devices. Fig. 8b shows the absorbance spectra of the films. The observed increase in absorbance with doping may stem from changes in the electronic structure or the formation of defect states induced by V incorporation.

The energy bandgap of the TiO_2 thin films was estimated using the Tauc method, as illustrated in Fig. 8c. The Tauc relation is expressed by the following equation:[54,55]

$$(\alpha h\nu) = A(h\nu - E_g)^n \quad (4)$$

where $n = 1/2$ for direct allowed transitions and $n = 2$ for indirect transitions, A is a material-specific constant, h is Planck's constant, and α is the absorption coefficient, calculated using:[56,57]

$$\alpha = (1/e)\{\ln(1 - R)^2/T\} \quad (5)$$

The values of the resulting optical bandgap are given in Table 2.

A reduction in the bandgap energy is observed with increasing vanadium content. This narrowing is likely caused by the formation of oxygen vacancies and localized states associated with Ti^{3+} ions.[58–60] When oxygen vacancies occur, electrons localize around the vacancy sites, creating donor levels just below the conduction band. These Ti^{3+}-related states introduce intermediate energy levels within the bandgap. Transition metal doping, such as with vanadium, can further contribute to bandgap narrowing through lattice distortion and defect formation, including oxygen vacancies and impurity states.[61] This effect is clearly demonstrated by the reduced bandgap values with increasing dopant levels. A photocatalyst's

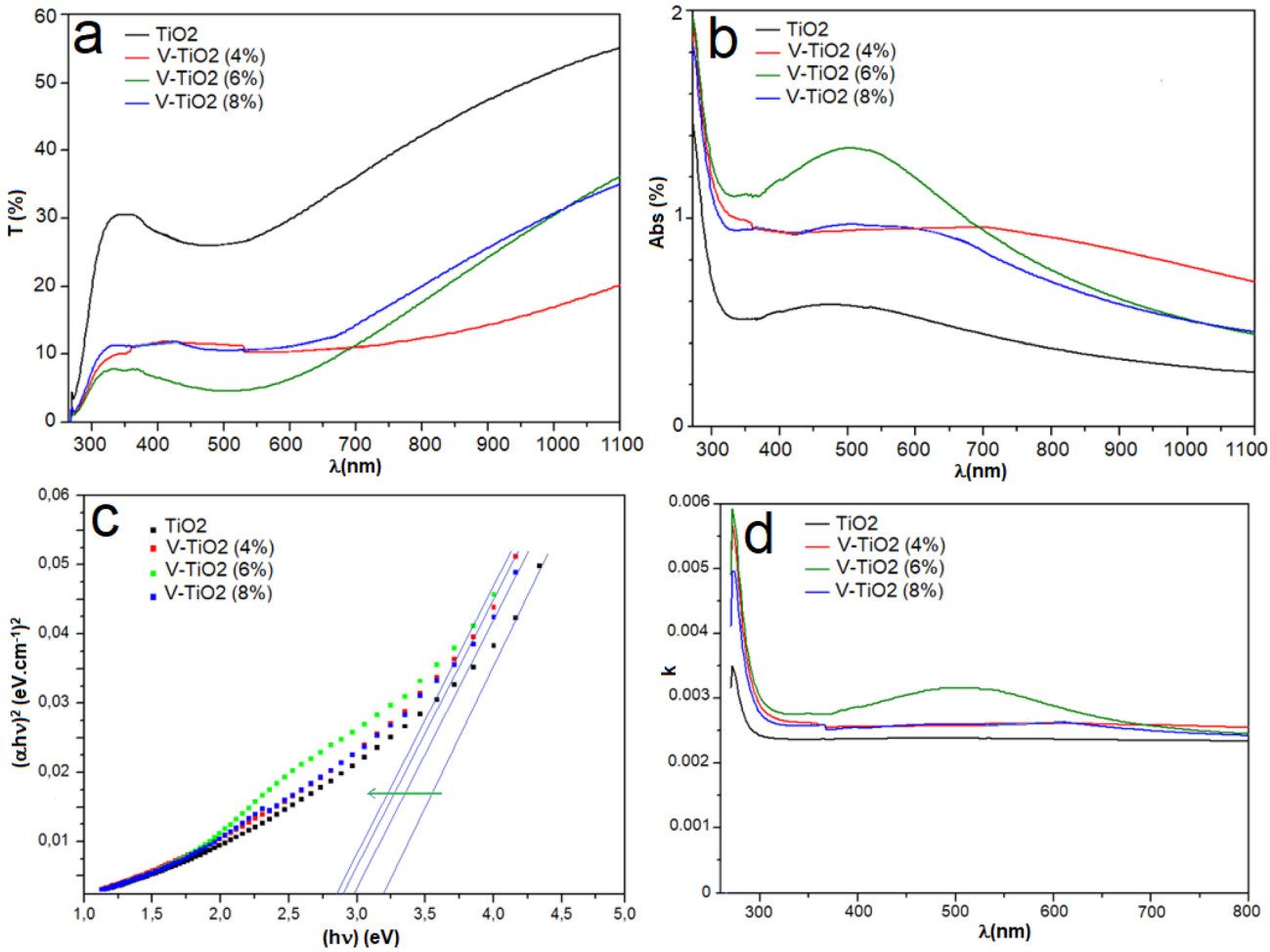

Fig. 8 Optical properties of undoped and vanadium-doped TiO_2 thin films: (a) transmission spectra, (b) absorbance spectra, (c) Tauc plots for bandgap estimation, and (d) variation of the extinction coefficient (k).

Table 2 Optical bandgaps of undoped and V-doped TiO_2 thin films at various doping levels

Thin layers	Gap energy (eV)
TiO_2	3.20
4% V-doped TiO_2	2.90
6% V-doped TiO_2	2.85
8% V-doped TiO_2	3.00

activity under solar irradiation is greatly increased when its bandgap is decreased, which makes it possible for it to absorb visible light more effectively. However, other material parameters such as particle size, morphology, and surface area also play a role in modulating the bandgap in semiconductor materials.

Fig. 8d shows the variation of the extinction coefficient (k) with wavelength in the 250–800 nm range for both undoped and V-doped TiO_2 films. The extinction coefficient was determined using the relation:[62]

$$K = (\alpha\lambda/4\pi) \quad (6)$$

As evident from the figure, the extinction coefficient increases in the 330–800 nm range for both pure and doped samples. The introduction of vanadium dopants is further enhanced, reflecting a corresponding rise in the absorption coefficient. This increase is attributed to the creation of shallow trap states within the band structure due to vanadium incorporation, which promotes additional photon absorption and thus lowers the optical bandgap, as illustrated in Fig. 9.[63]

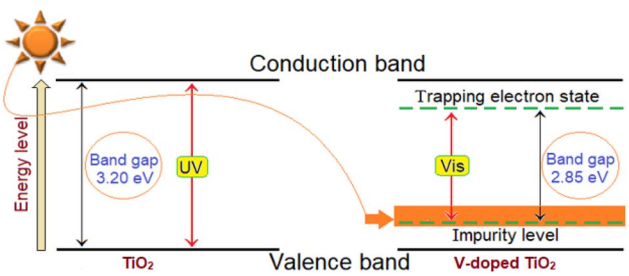

Fig. 9 Hypothetical optical band gap of undoped and doped V-TiO_2 thin films.

Developing composite materials or engineering defects to improve performance and stability are two ways to overcome the limitations of vanadium doping and its application under circumstances. High-level theoretical computations can be investigated, novel materials can be designed using machine learning, and new structures such as ultrathin or two-dimensional vanadium oxides can be created.

4 Conclusion

This study investigated the effects of vanadium doping on the structural, optical, and dielectric properties of TiO_2 thin films. XRD confirmed the anatase phase with enhanced crystallinity and reduced crystallite size upon doping. XPS analysis indicated the formation of Ti^{3+} states and oxygen vacancies, which play a key role in modifying optical and electronic behavior. SEM images showed uniform, spherical nanoparticles with increasing homogeneity at higher doping levels. Optical studies revealed a bandgap narrowing from 3.20 eV (undoped) to 2.85 eV (6% V-doped), attributed to intermediate states and increased disorder. The extinction coefficient increased across the visible range, reflecting enhanced light absorption. Dielectric measurements showed a high dielectric constant at low frequencies, influenced by porosity and space charge effects. Impedance analysis indicated thermally activated conduction and non-Debye behavior. Overall, vanadium doping effectively tunes the optoelectronic properties of TiO_2, making it a strong candidate for energy storage and photocatalytic applications. To further improve the performance of TiO_2 materials, further study could focus on co-doping, preparation process optimization, or classical simulations.

Author contributions

All authors contributed to conceptualization, methodology, writing original draft, writing review & editing, and formal techniques to analyze or synthesize study data.

Conflicts of interest

There are no conflicts to declare.

Data availability

This is to certify that all required and available data supported the work are included in the manuscript as figures and tables.

Acknowledgements

The authors extend their appreciation to Umm Al-Qura University, Saudi Arabia for funding this research work through grant number: 25UQU4280406GSSR03.

References

1 S. Yamazaki, S. Matsunaga and K. Hori, Photocatalytic degradation of trichloroethylene in water using TiO_2 pellets, *Water Res.*, 2001, **35**(4), 1022–1028.
2 H. Zhang, X. Ji, H. Yao, Q. Fan, B. Yu and J. Li, Review on efficiency improvement effort of perovskite solar cell, *Sol. Energy*, 2022, **233**, 421–434.
3 A. Romeo and E. Artegiani, CdTe-based thin film solar cells: past, present and future, *Energies*, 2021, **14**, 1684.
4 S. Ngqoloda, T. Ngwenya and M. Raphulu, *Recent Advances on the Deposition of Thin Film Solar Cells*, IntechOpen, London, UK, 2025.
5 J. Ramanujam, D. M. Bishop, T. K. Todorov, O. Gunawan, J. Rath, R. Nekovei, *et al.*, Flexible CIGS, CdTe and a-Si:H based thin film solar cells: a review, *Prog. Mater. Sci.*, 2020, **110**, 100619.
6 J. Tao, X. Hu, J. Xue, Y. Wang, G. Weng, S. Chen, *et al.*, Investigation of electronic transport mechanisms in Sb_2Se_3 thin-film solar cells, *Sol. Energy Mater. Sol. Cells*, 2019, **197**, 1–6.
7 J. Aljuaid, A. Timoumi and S. N. Alamri, Investigation of the impact of iron amounts on optical and physical properties of coated TiO_2 thin films used for PV solar cells, Optical Materials: X, *Opt. Mater.:X*, 2022, **16**, 100178.
8 L. Ryan, *Optical Analysis of Titania: Band Gaps of Brookite, Rutile and Anatase*, Department of Physics, Oregon State University, 2018.
9 A. Alotaibi, B. Williamson, S. Sathasivam, A. Kafizas, M. Alqahtani, C. Sotelo-Vazquez, *et al.*, Enhanced photocatalytic and antibacterial ability of Cu-doped anatase TiO_2 thin films: theory and experiment, *ACS Appl. Mater. Interfaces*, 2020, **12**(13), 15348–15361.
10 M. Liu, L. Zheng, X. Bao, Z. Wang, P. Wang, Y. Liu, *et al.*, Substrate-dependent ALD of Cu_x on TiO_2 and its performance in photocatalytic CO_2 reduction, *Chem. Eng. J.*, 2021, **405**, 126654.
11 Y. Zhang and W. Chu, Bisphenol S degradation via persulfate activation under UV-LED using mixed catalysts: synergistic effect of Cu–TiO_2 and Zn–TiO_2 for catalysis, *Chemosphere*, 2022, **286**(2), 131797.
12 P. Narayanama and S. Major, Langmuir-Blodgett based growth of rGO wrapped TiO_2 nanostructures and their photocatalytic performance, *Colloids Surf., A*, 2021, **609**, 125652.
13 R. Katal, S. Masudy-Panah, M. Tanhaei, M. H. Davood Abadi Farahani and H. Jiangyong, A review on the synthesis of the various types of anatase TiO_2 facets and their applications for photocatalysis, *Chem. Eng. J.*, 2020, **384**, 123384.
14 J. Zhang, *et al.*, Enhanced visible-light photoactivity of V-doped TiO_2 photocatalysts prepared by sol-gel method, *J. Mol. Catal. A: Chem.*, 2009, **304**(1–2), 28–33.
15 A. Timoumi, Reduction band gap energy of TiO_2 assembled with graphene oxide nanosheets, *Graphene*, 2018, **7**(4), 31–38.

16 R. Vidhya, R. Gandhimathi, M. Sankareswari, P. Malliga, J. Jeya and K. Neivasagam, Synthesis and characterization of Cu-doped TiO_2 thin films to protect agriculturally beneficial *Rhizobium* and *Phosphobacteria* from UV light, *J. Nanostruct.*, 2018, **8**(3), 232–241.

17 D. Jiang, Y. Ouyang, T. Otitoju, Y. Ouyang, N. Shoparwe, D. Zhang, *et al.*, A review on metal ions modified TiO_2 for photocatalytic degradation of organic pollutants, *Catalysts*, 2021, **11**, 1039.

18 K. Albaidani, A. Timoumi, W. Belhadj, S. N. Alamri and S. A. Ahmed, Structural, electronic and optical characteristics of TiO_2 and Cu-TiO_2 thin films produced by sol-gel spin coating, *Ceram. Int.*, 2023, **49**(22), 36265–36275.

19 G. Nagaraj, M. Mohammed, H. Abdulzahra, P. Sasikumar, S. Karthikeyan and S. Tamilarasu, Effects of the surface on solar-light photocatalytic activity of Ag-doped TiO_2 nanohybrid material prepared with a novel approach, *Appl. Phys. A*, 2021, **127**, 269.

20 Y. Hu, *et al.*, Photocatalytic activity of V^+-doped TiO_2 thin films prepared by sol-gel method, *J. Alloys Compd.*, 2008, **461**(1–2), 455–459.

21 T. Rajaramanan, S. Shanmugaratnam, V. Gurunanthanan, S. Yohi, D. Velauthapillai, P. Ravirajan, *et al.*, Cost effective solvothermal method to synthesize Zn-doped TiO_2 nanomaterials for photovoltaic and photocatalytic degradation applications, *Catalysts*, 2021, **11**, 690.

22 M. Abbas and M. Rasheed, Solid state reaction synthesis and characterization of Cu-doped TiO_2 nanomaterials, *J. Phys.: Conf. Ser.*, 2021, **1795**, 012059.

23 F. S. S. Zahid, M. S. P. Sarah, M. Z. Musa, U. M. Noor and M. Rusop, Electrical and optical properties of nanohybrid MEH-PPV: niobium doped TiO_2 thin films for organic photovoltaic cells, in *IEEE International Conference on Electronics Design, Systems and Applications (ICEDSA)*, 2012, pp. 22–26.

24 X. Wang, *et al.*, Visible-light photocatalytic activity in V-doped TiO_2 nanoparticles, *Appl. Surf. Sci.*, 2012, **258**(7), 2475–2480.

25 C. G. Wu, C. C. Chao and F. T. Kuo, Enhancement of the photo catalytic performance of TiO2 catalysts via transition metal modification, *Catal. Today*, 2004, **97**, 103.

26 S. Klosek and D. Raftery, Visible light driven V-doped TiO2 photocatalyst and its photooxidation of ethanol, *J. Phys. Chem. B*, 2001, **105**, 2815.

27 M. Anpo, S. Dohshi, M. Kitano, Y. Hu, M. Takeuchi and M. Matsuoke, The preparation and characterization of highly efficient titanium oxide-based photofunctional mate rial, *Annu. Rev. Mater. Res.*, 2005, **35**, 1.

28 J. Zhou, M. Takeuchi, A. K. Ray, M. Anpo and X. S. Zhao, Enhancement of photocatalytic activity of P25 TiO2 by vanadium-ion implantation under visible light irradiation, *J. Colloid Interface Sci.*, 2007, **311**, 497.

29 R. S. Ganesh, A. Y. Mamajiwala, E. Durgadevi, M. Navaneethan, S. Ponnusamy, C. Y. Kong, *et al.*, Zn and Sr co-doped TiO_2 mesoporous nanospheres as photoanodes in dye sensitized solar cell, *Mater. Chem. Phys.*, 2019, **234**, 259–267.

30 A. L. Patterson, The Scherrer formula for X-ray particle size determination, *Phys. Rev.*, 1939, **56**(10), 978–982.

31 Y. Wang, L. Zhang, S. Li and P. Jena, Polyol-mediated synthesis of ultrafine TiO_2 nanocrystals and tailored physiochemical properties by Ni doping, *J. Phys. Chem. C*, 2009, **113**(21), 9210–9217.

32 X. Gan, X. Li, X. Gao, J. Qiu and F. Zhuge, TiO_2 nanorod arrays functionalized with In_2S_3 shell layer by a low-cost route for solar energy conversion, *Nanotechnology*, 2011, **22**(30), 305601.

33 J. Z. Lu, Z. Zhou, Y. H. Wang, J. Li and X. Wei, Platinum-enhanced amorphous TiO_2-filled mesoporous TiO_2 crystals for the photocatalytic mineralization of tetracycline hydrochloride, *J. Hazard. Mater.*, 2019, **373**, 278–284.

34 Z. Han, C. Choi, S. Hong, T. S. Wu, Y. L. Soo, Y. Jung, *et al.*, Activated TiO_2 with tuned vacancy for efficient electrochemical nitrogen reduction, *Appl. Catal. B Environ.*, 2019, **257**, 117896.

35 R. Sanjinés, H. Tang, H. Berger, *et al.*, Electronic structure of anatase TiO_2 oxide, *J. Appl. Phys.*, 1994, **75**, 2945–2951.

36 J. G. Huang, X. T. Guo, B. Wang, L. Y. Li, M. X. Zhao, L. L. Dong, X. J. Liu and Y. T. J. Huang, Spectroscopic study of TiO_2-based nanomaterials, *Spectrochim. Acta, Part A*, 2015, **139**, 1–8.

37 H. Liao, L. Xie, Y. Zhang, X. Qiu, S. Li, Z. Huang, *et al.*, Mo-doped gray anatase TiO_2: lattice expansion for enhanced sodium storage, *Electrochim. Acta*, 2016, **219**, 227–234.

38 O. Avilés-García, J. Espino-Valencia, R. Romero, J. L. Rico-Cerda, J. Arroyo-Albiter, *et al.*, W and Mo doped TiO_2: synthesis, characterization and photocatalytic activity, *Fuel*, 2017, **198**, 31–41.

39 L. D. Li, J. Q. Yan, T. Wang, Z. J. Zhao, J. Zhang, J. L. Gong, *et al.*, Sub-10 nm rutile titanium dioxide nanoparticles for efficient visible-light-driven photocatalytic hydrogen production, *Nat. Commun.*, 2015, **6**, 5881.

40 H. Y. Gao, G. X. Hu, J. Sui, C. Mu, W. F. Shangguan, M. Kong, *et al.*, Scalable preparation of defect-rich free-standing TiO_2 sheets with visible-light photocatalytic activity, *Appl. Catal., B*, 2018, **226**, 337–345.

41 T. F. Khoon, J. Hassan, Z. Abd Wahab and R. S. Azis, Electrical conductivity and dielectric behaviour of manganese and vanadium mixed oxide prepared by conventional solid state method, *Eng. Sci. Technol.*, 2016, **19**(4), 2081–2087.

42 S. Khosravi, V. K. Veerapandiyan, R. Vallant and K. Reichmann, Effect of processing conditions on the structural properties and corrosion behavior of TiO_2–SiO_2 multilayer coatings derived via the sol-gel method, *Ceram. Int.*, 2020, **46**(11), 17741–17751.

43 L. N. Liu, C. C. Wang, D. M. Zhang, Q. L. Zhang, K. J. Wang, J. Wang, *et al.*, Dielectric relaxations and phase transition in laser crystals Gd_2SiO_5 and Yb-doped Gd_2SiO_5, *J. Am. Ceram. Soc.*, 2014, **97**, 1823–1828.

44 L. Tong, J. Sun, S. T. Wang, Y. M. Guo, Q. J. Li, H. Wang, *et al.*, Colossal dielectric behavior and dielectric anomalies in Sr_2TiCrO_6 ceramics, *RSC Adv.*, 2017, **7**, 50680–50687.

45 X. Zhao, X. D. Chen, X. Yu, X. Ding, X. L. Yu and K. Tang, High sensitivity humidity sensor and its application in nondestructive testing for wet paper, *Sens. Actuators, B*, 2019, **301**, 127048.

46 G. Wang, C. Wang, J. Zheng, S. Wang, R. Ahmed, J. Sun, *et al.*, Colossal and anomalous dielectric behavior in grain-oriented TiO_2, *J. Mater. Sci.*, 2020, **55**, 3940–3950.

47 D. C. Sinclair and A. R. West, Impedance and modulus spectroscopy of semiconducting $BaTiO_3$ showing positive temperature coefficient of resistance, *J. Appl. Phys.*, 1989, **66**, 3850–3856.

48 R. J. Álvaro, N. D. Diana and A. M. María, Impedance analysis of TiO_2 nanoparticles prepared by green chemical mechanism, *Contemp. Eng. Sci.*, 2018, **11**(15), 737–744.

49 J. Bashir and R. Shaheen, Structural and complex AC impedance spectroscopic studies of A_2CoNbO_6 (A = Sr, Ba) ordered double perovskites, *Solid State Sci.*, 2011, **13**(5), 993–999.

50 B. A. Bregadiolli, S. L. Fernandes and C. F. de Oliveira, Graeff. Easy and fast preparation of TiO_2-based nanostructures using microwave-assisted hydrothermal synthesis, *Mater. Res.*, 2017, **20**(4), 912–919.

51 S. Sahoo, U. Dash, S. K. S. Parashar and S. M. Ali, Frequency and temperature dependent electrical characteristics of $CaTiO_3$ nano-ceramic prepared by high-energy ball milling, *J. Adv. Ceram.*, 2013, **2**(3), 291–300.

52 B. Tanmaya, H. R. Kumar, N. S. Sekhar, M. Avinna and A. Sahid, Frequency and temperature dependence behaviour of impedance, modulus and conductivity of $BaBi_4Ti_4O_{15}$ Aurivillius ceramic, *Process. Appl. Ceram.*, 2014, **8**(3), 145–153.

53 E. Alamoudi and A. Timoumi, The synthesis and the effect of Cu on optoelectronic qualities of β-In2S3 as a window layer for CIGS thin film solar cells, *Results Phys.*, 2022, **40**, 105858.

54 N. Bouguila, A. Timoumi, H. Bouzouita, E. Lacaze, H. Bouchriha and B. Rezig, Molar ratio S/In effect on properties of sprayed In2S3 films, *Eur. Phys. J. Appl. Phys.*, 2013, **63**, 20301.

55 A. Akkari, C. Guasch, M. Castagne and N. Kamoun-Turki, Optical study of zinc blende SnS and cubic In_2S_3:Al thin films prepared by chemical bath deposition, *J. Mater. Sci.*, 2011, **46**, 6285–6292.

56 P. Mandal, U. P. Singh and S. Roy, Optical performance of europium-doped β gallium oxide PVD thin films, *J. Mater. Sci.: Mater. Electron.*, 2021, **32**, 3958–3965.

57 G. Charrada, M. Ajili, S. Bernardini, K. Aguir and N. Kamoun, Dual-functional green facile synthesis of graphene-doped CuO–SnO_2:F sprayed thin film as an efficient photocatalyst and ammonia gas sensor at low concentration, *Ceram. Int.*, 2025, **51**(16), 21326–21339.

58 X. Liu, S. Gao, H. Xu, Z. Lou, W. Wang, B. Huang, *et al.*, Green synthetic approach for Ti^{3+} self-doped TiO_{2-x} nanoparticles with efficient visible light photocatalytic activity, *Nanoscale*, 2013, **5**, 1870–1875.

59 X. Pan, M. Q. Yang, X. Fu, N. Zhang and Y. J. Xu, Defective TiO_2 with oxygen vacancies: synthesis, properties and photocatalytic applications, *Nanoscale*, 2013, **5**, 3601–3614.

60 S. Kalathil, M. M. Khan, S. A. Ansari, J. Lee and M. H. Cho, Band gap narrowing of titanium dioxide (TiO_2) nanocrystals by electrochemically active biofilms and their visible light activity, *Nanoscale*, 2013, **5**, 6323–6326.

61 Y. Zhang and X. Xu, Predicting thrust force during drilling of composite laminates with step drills through the Gaussian process regression, *ACS Omega*, 2020, **5**, 15344–15352.

62 Y. Al-Ramadin, Optical properties of poly (vinyl chloride)/poly (ethylene oxide) blend, *Opt. Mater.*, 2000, **14**, 287–290.

63 C. Y. W. Lin, D. Channei, P. Koshy, A. Nakaruk and C. C. Sorrell, Effect of Fe doping on TiO_2 films prepared by spin coating, *Ceram. Int.*, 2012, **38**, 3943–3946.